PAPER

Results from the Alfvén Eigenmode Active Diagnostic during the 2019-2020 JET deuterium campaign

Results from the Alfvén Eigenmode Active Diagnostic during the 2019-2020 JET deuterium campaign

R A Tinguely[1] [ORCID]**, P G Puglia[2], N Fil[3], S Dowson[3], M Porkolab[1], A Fasoli[2]** [ORCID]**, D Testa[2] and JET Contributors[4]**

[1] Plasma Science and Fusion Center, Massachusetts Institute of Technology, Cambridge, MA, United States of America
[2] Swiss Plasma Center, Ecole Polytechnique Fédérale de Lausanne, CH-1015 Lausanne, Switzerland
[3] Culham Centre for Fusion Energy, Culham Science Centre, Abingdon, United Kingdom
[4] See author list of E Joffrin *et al* 2019 Nucl. Fusion 59 112021

E-mail: rating@mit.edu

CrossMark

Abstract

This paper presents results of extensive analysis of mode excitation observed during the operation of the Alfvén Eigenmode Active Diagnostic (AEAD) in the JET tokamak during the 2019-2020 deuterium campaign. Six of eight toroidally spaced antennas, each with independent power and phasing, were successful in actively exciting *stable* MHD modes in 479 plasmas. In total, magnetic resonances were detected with up to fourteen fast magnetic probes. In this work, we present the calculations of resonant frequencies f_0, damping rates $\gamma < 0$, and toroidal mode numbers n, spanning the parameter ranges $f_0 \approx$ 30–250 kHz, $-\gamma \approx$ 0–13 kHz, and $|n| \leq 30$. In general, good agreement is seen between the resonant and the calculated toroidal Alfvén Eigenmode frequencies, and between the toroidal mode numbers applied by the AEAD and estimated of the excited resonances. We note several trends in the database: the probability of resonance detection decreases with plasma current and external heating power; the normalized damping rate increases with edge safety factor but decreases with external heating. These results provide key information to prepare future experimental campaigns and to better understand the physics of excitation and damping of Alfvén Eigenmodes in the presence of alpha particles during the upcoming DT campaign, thereby extrapolating with confidence to future tokamaks.

Keywords: Alfvén eigenmodes, stability, damping rate, toroidal mode number, fast magnetics

(Some figures may appear in colour only in the online journal)

1. Introduction

In tokamaks, an energetic particle (EP) population, such as radio frequency (RF) heated ions or DT alphas, can destabilize Alfvén Eigenmodes (AEs). In turn, these AEs can lead to an increase in EP transport and decrease in fusion performance. Understanding AE stability, i.e. driving and damping mechanisms, is therefore essential to the operation and success of future tokamaks with significant alpha particle populations, such as ITER [1], SPARC [2], and other devices.

In the JET tokamak, fast ion populations, such as those resulting from ion cyclotron resonance heating, can destabilize Toroidal Alfvén Eigenmodes (TAEs). These unstable modes are typically easily identifiable as coherent structures, with well-defined frequencies and toroidal mode numbers, in the Fourier spectra of fast magnetic probe data. For unstable AEs, their total growth rate is positive, $\gamma > 0$, as the fast ion drive overcomes various damping mechanisms, e.g. continuum, radiative, and electron/ion Landau damping. However, in the case of overwhelming damping, AEs cannot be

1

seen in the magnetic spectra without external excitation; this scenario may even occur in upcoming JET DT experiments if the alpha particle population is insufficient to destabilize the modes. Thus, in order to better study and understand AE stability, the Alfvén Eigenmode Active Diagnostic (AEAD, or AE antenna) [3, 4] is used in JET to actively excite, or probe, *stable* AEs and measure their resonant frequencies $\omega_0 = 2\pi f_0$, toroidal mode numbers *n*, and *total* damping rates $\gamma < 0$.

In this paper, we provide an overview of the operation and measurements of the AE antenna during the 2019-2020 JET deuterium campaign. We note that many past works have analyzed or reported data from previous campaigns; these include studies with the original, low-*n* saddle coils [1, 3, 5–23], the intermediate-to-high-*n*, eight antenna system [24–32], and the most recent upgrade [4, 33, 34], among others. Novel to this work are the following: (i) The recently upgraded independent phasing of the eight AE antennas allows probing of high toroidal mode numbers $|n| \leq 20$. (ii) An updated magnetics system, with fourteen fast magnetic probes, allows confident measurements of f_0, γ, and $|n| \leq 30$. (iii) A database of ~5000 resonances are detected in ~500 plasmas spanning a wide parameter space; important trends are observed in the bulk data, and identification of individual pulses opens opportunities for further study and comparison with simulation. These analyses are necessary for assessing AE drive and damping mechanisms, validating modeling efforts, and extrapolating the impact of AEs in future tokamaks.

The outline of the rest of the paper is as follows: In section 2, we briefly review active excitation of Alfvén modes with the AE antenna . Section 3 describes resonance detection with the fast magnetics system and details the calculations of f_0, γ/ω_0, and *n*. In section 4, we further explore operational and parameter spaces, noting trends in the data and suggesting opportunities for further analysis. Finally, a summary is provided in section 5.

2. Active antenna excitation

The original AE antenna system consisted of saddle coils capable of exciting AEs with low toroidal mode numbers $|n| \leq 2$ [3, 6]. From 2007-2008, an upgrade [24, 35, 36] involved the installation of eight in-vessel, toroidally spaced antennas - two sets of four - situated below the midplane at $R \approx 3.68$ m, $Z \approx -0.65$ m and with toroidal positions $\phi \approx 0, 4.7, 9.4, 14.1, 180, 184.7, 189.4, 194.1$ degrees. Each antenna comprises 18 turns and has poloidal and toroidal dimensions ~20 cm × 20 cm. The antennas can be operated in three frequency ranges $f = 25 - 50$ kHz, $75 - 150$ kHz, and 125–250 kHz, with each frequency filter allowing antenna currents up to $I_{ant} \approx 10$A, 7A, and 4A, respectively, at the maximum frequencies. A synchronous detection system is used to identify [5] and track [7] resonances in real time.

To find stable AEs, the antennas' frequencies are simultaneously scanned within a given filter's range at rates $|df/dt| \leq$ 50 kHz s^{-1}, 100 kHz s^{-1}, and 200 kHz s^{-1}, respectively, for

the filters above. The operational space of the AE antenna during the 2019 JET deuterium campaign is visualized in figure 1(a); the histogram (black) shows the number of data points N_{bin} collected within each frequency bin, normalized to the total number of data points N_{tot}. (Throughout the paper, N_{tot} will be noted for each histogram or distribution.) Error bars - though impossible to see in the black histogram - are included to indicate the uncertainty from counting statistics, calculated here as $\sqrt{N_{bin}}/N_{tot}$. As can be seen, the system was operated more frequently with the high frequency filters, and no data exist in the inaccessible range $f = 50–75$ kHz. In total, the AE antenna was operated during 676 plasma discharges during the 2019-2020 deuterium campaign, spanning JPN $93063 - 96855$.

Following a recent system upgrade [4], six new amplifiers allow antennas 1–5 and 7 to be powered and phased independently. This marks a significant improvement over the previous AE antenna feed system, which had only 0 or π phasing. Now, antenna phases can be carefully chosen so that the injected power spectrum is maximal at toroidal mode numbers as high as $|n| \approx 20$. The operational space for the dominant applied toroidal mode number is shown in the normalized histogram (black) of figure 2(a). The antenna was operated most frequently with phases $n = 0, -1, -4$ and -10, with positive *n* defined in the direction of the plasma current I_p. These were effectively randomly chosen by the operators in order to probe even vs odd and low vs high toroidal mode numbers. The predominance of negative *n* values in the applied mode number was an operational oversight as I_p is typically directed in the $-\phi$ direction in JET. The calculation of *n* will be discussed in the following section.

3. Resonance detection and parameter estimation

As the antenna frequency passes through the AE resonant frequency, the plasma responds like a driven, damped harmonic oscillator. The resulting magnetic response is measured by a set of fourteen toroidally distributed fast magnetic probes, listed in table 1. This marks an improvement over past analyses for which only ten probes - or fewer - were available [32]. The magnetic signals are synchronously detected at the antenna frequency with an effective band-pass filter of width $\Delta f \approx 0.1$ kHz [7]. This gives a time-evolving amplitude and phase for each probe; for example, see those in figure 3(b). The data from all probes are then used to calculate the AE resonant frequency f_0, damping rate γ, and toroidal mode number *n*.

3.1. Resonant frequency and damping rate

For an driven, *weakly* damped harmonic oscillator, i.e. $|\gamma/\omega_0| \ll 1$, the system response to a driving frequency ω is well-approximated by the transfer function [3, 5, 38]

$$H(\omega) = \frac{1}{2}\left(\frac{r}{i(\omega - \omega_0) - \gamma} + \frac{r^*}{i(\omega + \omega_0) - \gamma}\right) + \text{offset}, \quad (1)$$
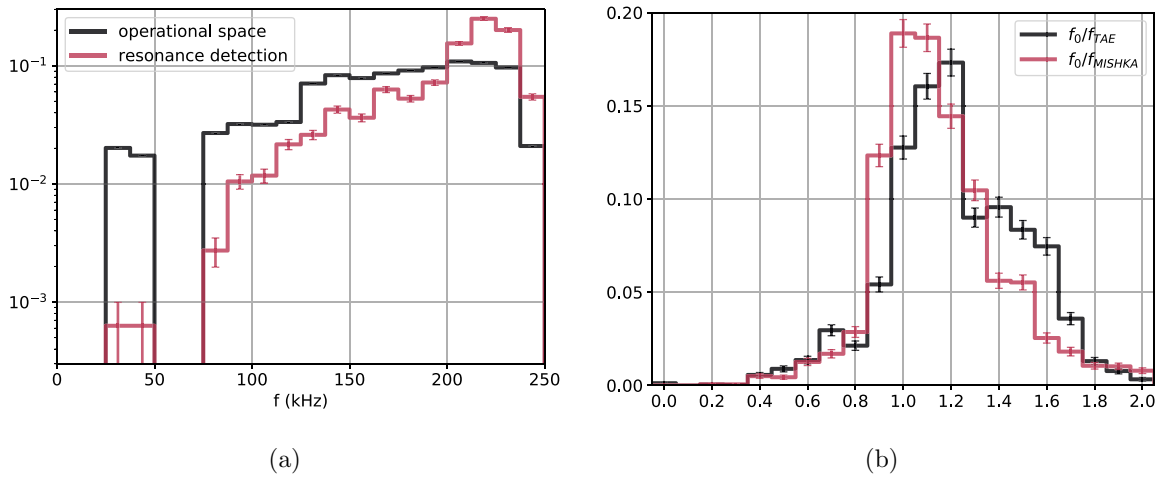
(a)   (b)

Figure 1. Histograms normalized to their total number of data points N_{tot}: (a) The antenna operational space ($N_{tot} \approx 5 \times 10^6$) and resonance detection space ($N_{tot} = 4768$) versus frequency. (Note the logarithmic scale of the vertical axis.) (b) Ratios comparing resonant, estimated TAE, and MISHKA-evaluated [37] frequencies ($N_{tot} = 3780$). Uncertainties are shown as error bars.
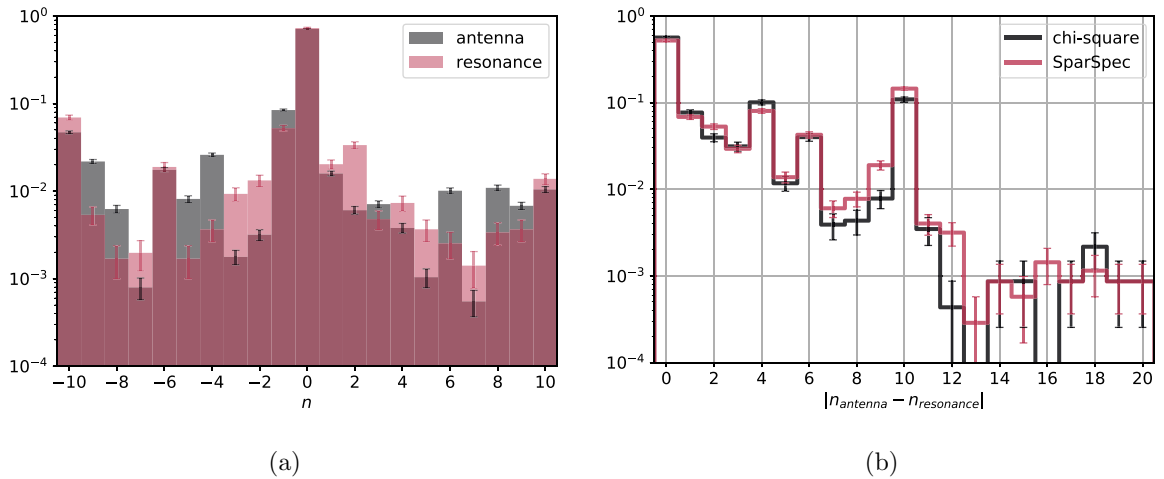

(a)   (b)

Figure 2. Histograms (normalized) of (a) toroidal mode numbers applied by the antenna ($N_{tot} = 17103$) and estimated of the resonances using SparSpec (see section 3.3.2, $N_{tot} = 3549$), and (b) the absolute difference between the applied antenna toroidal mode number and that estimated of each resonance using the chi-square (see section 3.3.1, $N_{tot} = 2328$) and SparSpec ($N_{tot} = 3505$) methods. All data are restricted to $|n| \leq 10$, and estimations require a 'confidence factor' $X \geq 2$ or $A \geq 2$ (see text for details). Uncertainties are shown as error bars.

Table 1. Fast magnetic probes and their toroidal positions rounded to the nearest degree. Those with names beginning with H or T are used to calculate the toroidal mode number.

Probe	H301	H302	H303	H304	H305	T001	T002	T006	T007	T008	T009	I801	I802	I803
Angle	77	93	103	108	110	3	42	183	222	257	290	317	317	318

with r a complex residue and * denoting the complex conjugate. The resulting pole in the complex plane can be seen in figure 3(b) for ten probes (see caption for details). A fit of equation (1) gives values $\omega_0 = 2\pi f_0$ and γ/ω_0 for each probe, along with associated uncertainties Δf_0 and $\Delta(\gamma/\omega_0)$. In this work, the final fitted values of f_0 and γ/ω_0 are calculated as the mean of all probes' fits with inverse variance weighting; here, the variance is taken to be the square of the uncertainty. The total uncertainty is then calculated as the standard error of the weighted mean in a way similar to [39], except that the inverse

variance is (again) used for weighting[5], which actually makes this estimation more conservative.

An automatic resonance detection algorithm was run on all 676 plasma pulses with AE antenna operation. Each probe was calibrated for its frequency-dependent response. The sum of all magnetic probes' amplitudes was used to identify peaks in signal - i.e. possible resonances - in an unbiased way. Selection

---

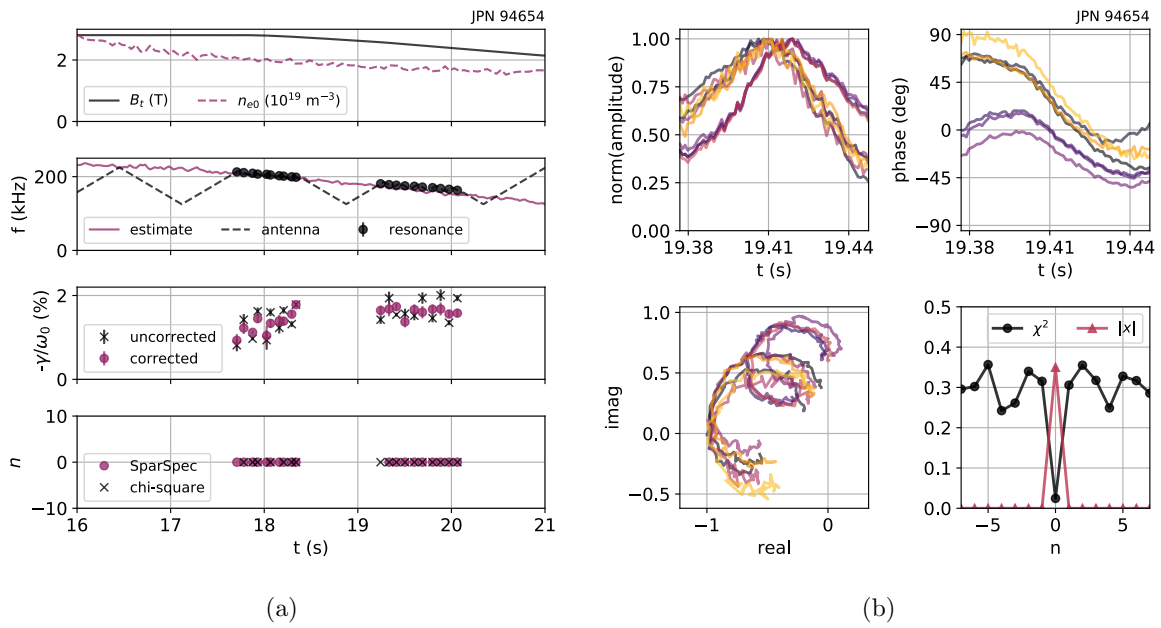[5] As opposed to the *square* of the inverse variance.

(a)

(b)

Figure 3. (a) The toroidal magnetic field and central electron density; estimated TAE, antenna, and resonant frequencies; uncorrected and corrected damping rates; and toroidal mode numbers calculated by both SparSpec and chi-square methods, with 'confidence factors' $X \geq 2$ and $A \geq 2$ (see text for details), for JPN 94654. (b) For one resonance, data from ten fast magnetics probes: amplitudes normalized to their maxima, phases (only those used for the toroidal mode number calculation), complex representations, and resulting chi-square and SparSpec amplitude spectra limited to $|n| \leq 7$. From table 1, probes used are H301-5, T006/7, and I801-3.

Table 2. Minimum constraints on data in this paper.

Parameter	Upper bound
Uncertainty in resonant frequency	$\Delta f_0 \leq 1$ kHz
Normalized damping rate	$-\gamma/\omega_0 \leq 6\%$
Uncertainty in damping rate	$\Delta(\gamma/\omega_0) \leq 1\%$
NBI power	$P_{NBI} \leq 7$ MW

criteria for the data to be fit with equation (1) include the following: The maximum amplitude of each peak must be at least 20% higher than its neighboring minima. The time duration of each peak must be in the range $\Delta t = 10$–200 ms, and a phase change of $\Delta\theta = 55$–180 degrees must occur[6]. Any fits with uncertainties $\Delta f_0 > 10$ kHz or $\Delta(\gamma/\omega_0) > 10\%$, or R-squared 'goodness of fit' $R^2 < 0.8$ are discarded outright. Of those remaining, data from at least three probes are needed to compute the weighted average. After this initial filter, data presented in this paper are also subject to the constraints of table 2: The first three constraints increase our confidence in the probes' collective measurement. The last constraint filters out noise due to high neutral beam injection (NBI) power and associated edge localized modes (ELMs), as done in [23]. However, note that there are novel measurements of stable TAEs at high external heating powers (NBI + RF) ~ 25 MW, which will be explored in future work.

In total, there were $N_{tot} = 4768$ resonances detected in 479 pulses which satisfied the above criteria. The frequencies of these resonances are shown in the histogram (purple) of figure 1(a). We see that the number of observations increases with frequency, with most having $f_0 \geq 200$ kHz, a typical range for TAE frequencies in JET. An estimate of the TAE frequency, calculated as $f_{TAE} \approx B_0/4\pi q_0 R_0 \sqrt{\mu_0 m_{eff} n_{e0}}$, is shown for pulse JPN 94654 in figure 3(a). Here, on-axis parameters are the toroidal magnetic field B_0, safety factor q_0, major radius R_0, and electron density n_{e0}; the vacuum permeability is μ_0, and effective mass is $m_{eff} \approx m_H(2 - n_H/n_e - n_{He3}/n_e)$, with m_H the mass of hydrogen. The estimated frequency f_{TAE} and resonant frequency f_0 agree well for JPN 94654, and the real-time resonance tracking system is also successfully demonstrated in this pulse.

The ratio of fitted resonant frequencies to their corresponding estimated TAE frequencies is shown in the histogram (black) of figure 1(b). The histogram peaks at a ratio of $f_0/f_{TAE} = 1.2$ and skews toward values $f_0/f_{TAE} > 1$, which has been observed for AE antenna data previously [6, 19]. This can be compared with the ratio of resonant frequencies to the TAE frequencies calculated by the MHD code MISHKA [37], also shown in figure 1(b) (purple). To calculate f_{MISHKA}, the code HELENA [40] was first used to convert the magnetic geometry from EFIT [41] into the format required by code CSCAS [42], which calculates the Alfvén continuum. Then MISHKA was used to calculate mode structures and final TAE frequency estimates for $n = 0$–7. The histogram of f_0/f_{MISHKA} uses the value of f_{MISHKA} with the same estimated $|n|$ as the resonance.

As expected, f_0 agrees better with f_{MISHKA} than f_{TAE}, although the histogram is still skewed toward $f_0/f_{MISHKA} > 1$.

---

[6] During real-time resonance tracking, the transitions between positive and negative antenna scan rates, i.e. $df/dt \to -df/dt$, can occur so quickly that only a small phase change, e.g. $\Delta\theta \approx 1$ rad ≈ 57 degrees, is observed.

One likely cause for this discrepancy is the uncertainty in the safety factor profile calculated by standard EFIT; this can be better constrained with Motional Stark Effect or Faraday rotation data, but such data were not available for every pulse. Plasma rotation will also shift the mode frequency with respect to the lab frame; however, because rotation was not regularly diagnosed, it has not been included in this analysis.

3.2. Damping rate correction

The transfer function of equation (1) is technically only valid for weakly damped harmonic oscillators with constant resonant and driving frequencies. This is not the case in these experiments as both the antenna and resonant frequencies are changing in time. For most cases, $|df_0/dt| \ll |df/dt|$, so this is no issue. However, when $|df_0/dt| \sim |df/dt|$, the resonant peak can appear much sharper or broader than the true damping rate would allow. Modifying equation (1) presents a challenge as the true differential equation representing the physical system now involves additional time dependencies $\omega(t)$ and $\omega_0(t)$. Even linear approximations, e.g. $\omega(t) \approx \omega + \alpha t$, introduce non-linearities which have no analytical solution.

Therefore, equation (1) was used for the calculation of all damping rates, and a correction was applied in post-processing, as has been done previously [7]. This corrective 'lookup table' was assembled in the following way: The amplitude and phase of a driven, damped harmonic oscillator were simulated for a range of 'true' damping rates and linearly varying driving and resonant frequencies, spanning all values in our database: $-\gamma/\omega_0 \in [0.1\%, 6\%]$, $(df_0/dt)/f_0 \in [0,1]\,\text{s}^{-1}$, and $(df/dt)/f_0 \in [-1.7, 1.7]\,\text{s}^{-1}$.[7] The resulting synthetic data were fit with 1 to create a map from 'true' to 'erroneous,' or corrected to uncorrected, damping rates. Finally, the total uncertainty was taken as the sum of corrected and uncorrected uncertainties in quadrature.

An example of the difference between corrected and uncorrected damping rates can be seen in figure 3(a). In JPN 94654, the AE antenna scan rate was $|df/dt| = 150\,\text{kHz}\,\text{s}^{-1}$, and the resonant frequency changed at a rate $-df_0/dt \approx 20 - 40\,\text{kHz}\,\text{s}^{-1}$ as determined from real-time tracking of the mode.[8] The uncorrected damping rate is observed to alternate between lower and higher values depending on the sign of df/dt. For most resonances, the corrected damping rate falls in between the two extremes and varies more smoothly in time. Unless otherwise noted, all damping rates reported in this paper are the corrected values, e.g. in figure 4.

3.3. Toroidal mode number

The toroidal mode number of the detected resonance is estimated using only those probes located on the outer wall at approximately the same radial and poloidal positions; these probes' names begin with H or T in table 1. Of the eleven available probes, at least three must have had 'good' resonance fits,

---

as described above, to be added to the database; thus, there are instances of resonances for which we are confident in the fitted values of f_0 and γ/ω_0, but have no estimate of n.

Following the standard convention [43], positive n are measured in the co-current, i.e. co-I_p, direction. In JET, the normal operating scenario is $I_p < 0$ and $B_0 < 0$, meaning both are directed clockwise ($\phi < 0$) when viewing the tokamak from above; this is the case for *all* pulses in our database. Thus, positive (negative) n are oriented clockwise (counter-clockwise). As mentioned, this also explains the operational preference for negative phasing (see figure 2(a)) which is in the $\phi > 0$ direction.

The toroidal mode number is perhaps the most difficult parameter to assess of a resonance due to the reliance on multiple probes, possible superposition of modes, and aliasing effects. Yet knowing the toroidal mode number is critical to studying n-dependent AE stability. Past analyses of AE antenna data have used several different methods to calculate n, including linear fitting [18] and sparse spectral decomposition [22–32]. In the following sections, we pursue two complementary methods of n evaluation: The first is a weighted chi-square calculation using only phase information; the second utilizes the SparSpec algorithm [22] to decompose both probe amplitude and phase information. Agreement between the methods gives us reassurance that the result is correct; disagreement provides motivation for further investigation. In the latter case, SparSpec can help identify sub-dominant modes which may also have good - though not the best - chi-square fits.

3.3.1. Chi-square evaluation.
For the first method, we minimize a weighted, reduced chi-square spectrum within the range of resolvable toroidal mode numbers. For N 'good' probes and a range of toroidal mode numbers $n \in [-n_{\max}, n_{\max}]$, the reduced chi-square spectrum is computed as

$$\chi^2(n) = \frac{1}{N^2} \sum_{i=1}^{N} \left[\sum_{j=1}^{N} \frac{\min\{[n(\phi_j - \phi_i) - \theta_j]^2\}}{\sigma_j^2} \middle/ \sum_{j=1}^{N} \frac{1}{\sigma_j^2} \right].$$

(2)

Here, ϕ_j is the toroidal position of each probe j (see table 1), θ_j is the corresponding phase angle of the probe signal at the resonant frequency $f = f_0$, and the inverse variance weighting uses the uncertainty of the normalized damping rate measurement $\sigma_j = \Delta(\gamma/\omega_0)$. The inner sum over all probes j is the typical chi-square calculation, while the outer sum over all probes i allows each probe to be considered the reference at the origin $\phi = 0$. Note that *minimum* difference between angles is used in the actual computation, since ϕ and θ are periodic in 2π.

The range of resolvable toroidal mode numbers, $|n| \leq n_{\max}$, depends on the probes used in each evaluation of equation (2). As shown in appendix A, the theoretical $n_{\max}$ is equal to the least common denominator of all probe positions ϕ_i/π, assuming that these are rational numbers and that one probe is at the origin $\phi_1 = 0$. In practice, $n_{\max}$ can be computed through brute

---

[7] For $(df_0/dt)/f_0 < 0$, the signs of df_0/dt and df/dt can be flipped.

[8] For isolated resonances, i.e. no real-time tracking, df_0/dt is calculated from the estimated f_{TAE}.

force by comparing each n of interest. In this work, we allow a generous uncertainty in the phase, $\Delta\theta = 30$ degrees, which makes our estimate more conservative. Sometimes, n_{max} and $-n_{max}$ are indistinguishable; in this case, the range defaults to $n \in [-n_{max} + 1, \ldots, n_{max}]$. For this analysis, we cap the value at $n_{max} \leq 10$, although the true value is often $n_{max} \sim 20$ or greater. We have chosen this upper bound based on the toroidal mode numbers of *destabilized* TAEs observed in JET; for example, see those in figure 12 of [44].

The final estimate of the toroidal mode number n_0 is taken as the value which minimizes the chi-square spectrum, $\min[\chi^2(n)] = \chi^2(n_0)$, within a given range $|n| \leq n_{max}$. To quantify our confidence in this estimate, we define a 'confidence factor' X as

$$X = \frac{\min[\chi^2(n \neq n_0)]}{\chi^2(n = n_0)} \geq 1. \tag{3}$$

In other words, the minimum χ^2 value is smaller than all others in the spectrum by a factor X, and our confidence increases as X increases.

3.3.2. SparSpec evaluation.
Borrowing a technique [45] from the field of astronomy, the SparSpec code [22] utilizes the 'sparse' representation of signals—i.e. data from a limited set of unevenly spaced magnetic probes—and performs a spectral decomposition to find a superposition of toroidal modes. Details of this calculation [22, 45], its real-time implementation on JET [26, 28, 32], and associated analyses [23–25, 27, 29–31] can be found in a variety of references. A brief overview is given here: For N probes at toroidal positions $\phi = [\phi_1, \ldots, \phi_N]$, their complex-valued measurements can be represented as $\mathbf{y} = [y_1, \ldots, y_N]$. For a range of toroidal mode numbers n_j, a matrix can be created with complex-valued components $W_{jk} = \exp(in_j\phi_k)$. The aim is then to minimize the function

$$J(\mathbf{x}) = ||\mathbf{y} - W\mathbf{x}||^2 + \lambda \max(W^\dagger \mathbf{y}) \sum_j |x_j|, \tag{4}$$

where $\lambda \in [0, 1]$ is a free parameter, $W^\dagger$ is the conjugate transpose of W, and x_j is the fitted amplitude of mode n_j. When $\lambda = 0$, equation (4) is just a linear least-square fit; however, for $\lambda > 0$, the second term of equation (4) is a cost function penalizing additional non-zero amplitudes x_j.

In this work, we evaluated SparSpec over a range of toroidal mode numbers $|n| \leq 30$ with a cost function parameter $\lambda = 0.85$, a value found to work well in previous studies [26, 28]. In theory, this combination should lead to noise in the signal being 'filtered out' as low-level amplitudes at high mode numbers. Then, just as with the chi-square evaluation in the previous section, the range of toroidal mode numbers was limited to those resolvable by the available probes. In past works, this spectral decomposition was then used to compute the resonant frequency and damping rate of each individual mode contributing to the observed resonance. Here, for simplicity, we report the 'dominant' mode n_0 having the largest amplitude $|x_0| = \max(|x_j|)$. We compute another 'confidence

factor' A similar to 3, but comparing the maximum (absolute) amplitude to all others in the SparSpec spectrum, i.e.

$$A = \frac{|x_j(n_j = n_0)|}{\max |x_j(n_j \neq n_0)|} \geq 1. \tag{5}$$

In other words, the absolute amplitude of the dominant mode is greater than that of each other mode by this factor A, and our confidence increases as A increases.

3.3.3. Results.
Toroidal mode number estimates using both chi-square and SparSpec calculations, with confidence factors $X \geq 2$ and $A \geq 2$, respectively, are shown in figure 3(a) for JPN 94654. For this pulse, all estimates are $n_0 = 0$. The chi-square and SparSpec spectra are also shown for one resonance in figure 3(b); both show a 'confident' prediction of $n_0 = 0$. Since TAEs cannot have $n = 0$, this could indicate a measurement of a Global Alfvén Eigenmode (GAE) [46, 47] which has been observed previously in JET; see [7, 14, 29, 48] and others.

All resonances' toroidal mode numbers, evaluated with SparSpec and a confidence factor $A \geq 2$, are shown in the histogram (purple) of figure 2(a)[9]. As with the antenna operational space, most resonances are estimated to have $n = 0$, with the number of observations generally decreasing as $|n|$ increases. A similar trend was observed in past AE antenna data; see figure 3 in [29]. The predominance of $n = 0$ measurements has a few explanations: First, a subset of these could truly be GAEs, as mentioned. Additionally, there could be a superposition of modes dominated by $n = 0$; identifying subdominant modes via SparSpec will be explored in future work. Finally, as the number of magnetic probes with 'good' fits decreases, the range of resolvable n often decreases as well; this biases measurements toward low n.

The absolute difference between the applied antenna and estimated resonance mode numbers, $|n_{ant} - n_0|$, is shown in figure 2(b) for both chi-square and SparSpec evaluations with confidence factors $X \geq 2$ and $A \geq 2$, respectively. Importantly, figure 2(b) confirms the successful operation of the AE antenna. Recall that the antenna and resonant toroidal mode numbers are estimated in the same way, but ultimately come from two different sources: antenna currents and magnetic signals. The histogram is peaked at a difference of zero and decreases exponentially as the separation increases. Note the 'dips' at odd differences (i.e. $|n_{ant} - n_0| = 3, 5, \ldots$) and 'peaks' at even differences (i.e. $|n_{ant} - n_0| = 4, 6, \ldots$). This is caused by the discrete antenna system injecting power into a spectrum of toroidal modes, often preserving parity; for example, see the driven n-spectrum in figure 2 of [29]. Note that the salient peak at $|n_{ant} - n_0| = 10$ is an artifact due to the nearly $n = 10$ spacing of a subset of probes in table 1 [22, 23].

Finally, note that while we consider toroidal mode number estimations in range $|n| \leq 10$ to be most plausible, observations of $|n| > 10$ are still prevalent: ~ 60 measurements via the

---

[9] Note that a histogram of data from the chi-square evaluation is not shown in figure 2(a) because it is almost identical to - i.e. agrees well with - that from SparSpec.

chi-square method with $X \geq 2$ and ~ 200 measurements from SparSpec with $A \geq 3$. These will be investigated more carefully in future work.

4. Observations in plasma parameter space

In the previous section, we compared the operational space of the AE antenna with the resonances' parameter space. In this section, we comment on the plasma parameter space within which these resonances were observed. It is important to note that there are several layers to the exploration of this parameter space: First, there are data associated with only *observations* of resonances, such as the histogram of resonant frequencies in figure 1(a). Then there are observational data *normalized* to the antenna operational space. For example, we observed fewer resonances at low frequencies $f = 25–50$ kHz, but also operated the antenna less often in that frequency range. An even deeper layer could consider the *existence* of AEs (or other resonances) in any frequency range and the required accessibility of our antenna to probe them. However, to learn this accessibility/existence space would require extensive computational efforts and would be sensitive to many uncertainties, so it is not pursued in this paper.

Ranges of plasma parameters in our database are given in table 3. The 5th and 95th percentiles of each parameter distribution are denoted, meaning 5% and 95% of the distribution are less than these values, respectively. These can be compared to a similar database in [29]; see table 1 therein. Note that in [29] only ohmically heated plasmas were used to construct the database. Of the resonances in our data set, the proportions measured in limiter and X-point magnetic configurations were $\sim 17\%$ and $\sim 83\%$, respectively. Unless otherwise noted, data in this paper include both limiter and X-point configurations. The effects of plasma shaping and plasma-antenna coupling on AE measurements have been investigated in past works [1, 14, 20, 24, 25, 27, 29, 30, 32] and will be explored for our database in an upcoming study [49]. In this section, we highlight a few salient observations and trends, but note that extracting physics from the database will require careful data filtering, proper statistical analysis, and physics-based guidance.

The probability of resonance detection, normalized to the antenna operational space, is shown as a function of plasma current I_p in the histogram of figure 4(a). Each bin accounts for the number of resonance observations *and* the number of times the antenna operated within the bin's range. The error bars represent uncertainties from counting statistics of both values, propagated appropriately. Interestingly, there is a steep drop-off in the detection probability for plasma currents beyond $I_p > 2$ MA; that is, we were less likely to measure resonances when operating above 2 MA. The detection probability is actually zero for $I_p > 3$ MA. One explanation for this is that the (fixed) antenna currents have a lower perturbative effect as I_p increases. The driven magnetic perturbation by the antenna at the plasma edge is of order $\delta B \approx 0.1–1$G [4, 24]; therefore, a threefold increase in the poloidal field strength could reduce the antenna perturbation and/or plasma response

Table 3. Ranges of plasma parameters for the resonance database: plasma current, on-axis toroidal magnetic field, central electron density and temperature, NBI and RF heating powers, plasma-antenna separation, ELM frequency, central and edge safety factors, edge magnetic shear, elongation, upper and lower triangularities, normalized beta and internal inductance. Here, 5% of the distribution falls below the 5th percentile value; 95% falls below the 95th percentile.

Parameter	5th percentile	95th percentile
I_p (MA)	0.74	1.97
B_0 (T)	1.74	3.41
n_{e0} (10^{19} m^{-3})	1.52	4.73
T_{e0} (keV)	1.04	2.50
P_{NBI} (MW)	0.00	2.19
P_{RF} (MW)	0.00	2.86
d_{sep} (cm)	9.98	16.74
f_{ELM} (Hz)	0.00	14.30
q_0	0.84	2.21
q_{95}	3.21	7.79
s_{95}	3.00	5.81
κ	1.27	1.67
δ_u	0.00	0.25
δ_l	0.02	0.35
β_N	0.10	0.54
ℓ_i	1.00	1.70

$|\delta B / B|$ to below measureable levels. At the same time, there could be a variety of other conflating factors in these high performance discharges which contribute to this observation.

In figure 4(b), we show the probability of resonance detection, again normalized to the antenna operational space, as a function of heating power. We use wide bins, $\Delta P = 2$ MW, in our histogram for two reasons: (i) to improve statistics and (ii) because external heating is usually not varied continuously, but rather operated at fixed levels. For NBI heating only, the detection probability is relatively uniform for $P_{NBI} \leq 3.5$ MW, but drops sharply for higher powers. This could be explained by ion Landau damping from an increased population of NBI ions; such an effect has been noted before in JET [7, 17, 44]. In fact, the damping rate of $n = 1$ TAEs was found to decrease for $P_{NBI} = 0 − 3$ MW but increase beyond $P_{NBI} > 3$ MW in [17]. Note that the AE antenna was operated for heating powers up to $P_{NBI} \approx 30$ MW in the 2019-2020 campaign. However, as discussed previously, noise in the magnetics signals, such as that due to ELMs, is particularly prevalent for $P_{NBI} > 7$ MW and can be misidentified as resonant peaks. Therefore, these data were excluded, as has been done in previous AE antenna studies [23].

For RF heating only, the probability of resonance detection decreases sharply beyond $P_{RF} > 1.5$ MW. This finding is more difficult to interpret than for only NBI heating because RF-heated fast ions can both stabilize and destabilize AEs in JET. For example, in [7], increasing RF power was found to stabilize $n = 0$ GAEs (i.e. increase their damping rate), but destabilize $n = 1$ TAEs (i.e. decrease their damping rate). What can be inferred from figure 4(b) is that AE stability is more difficult to assess in high-power JET plasmas; therefore, AE
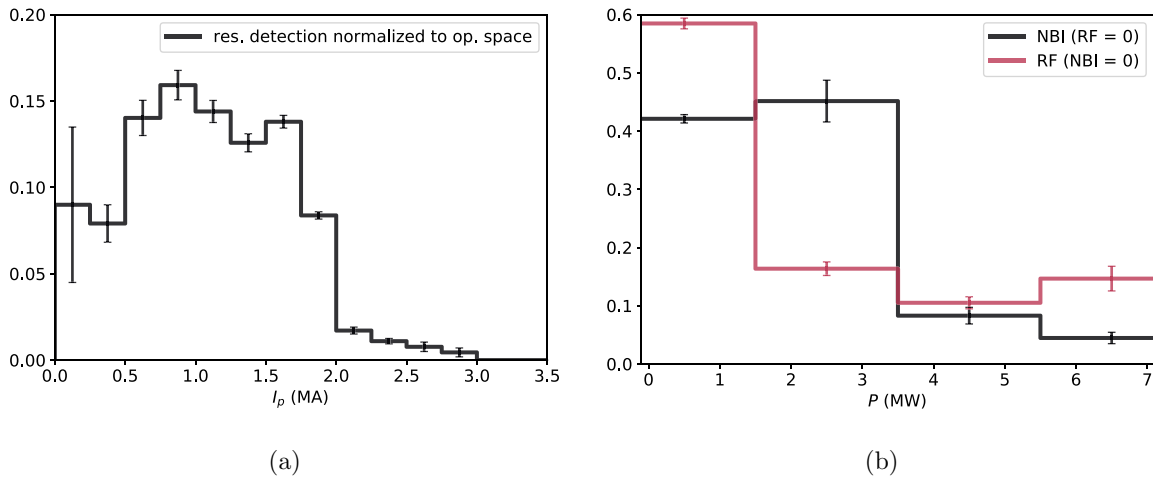
(a)   (b)

Figure 4. Histograms of the probability of resonance detection *normalized to the operational space* versus (a) plasma current ($N_{tot} = 4768$) and (b) NBI ($N_{tot} = 3777$) and RF ($N_{tot} = 4392$) heating powers. Uncertainties are shown as error bars.

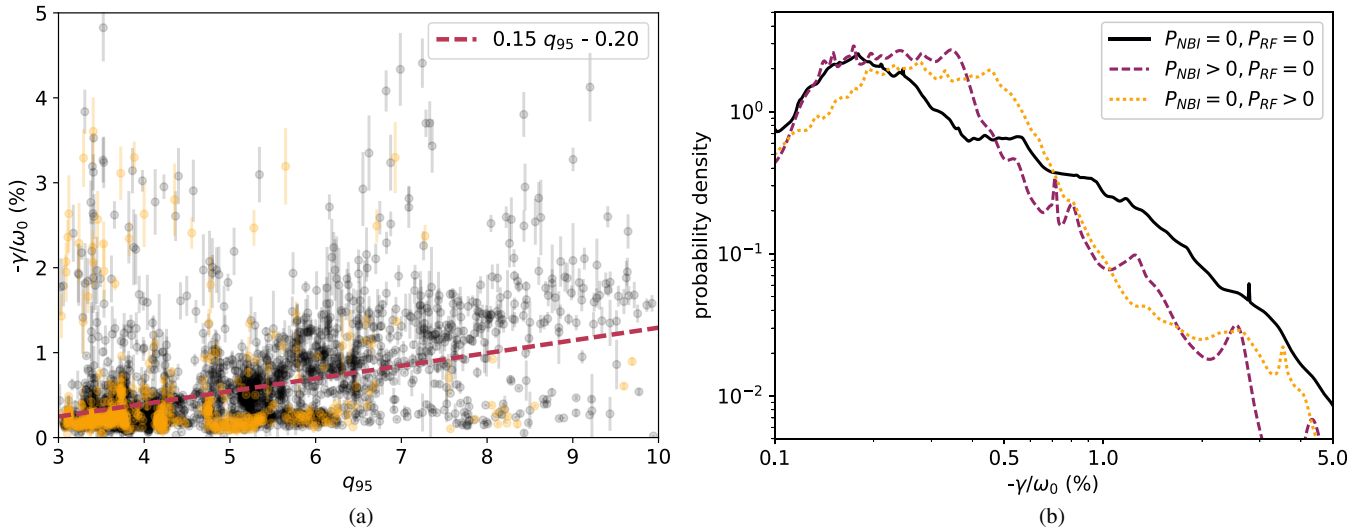(a)   (b)

Figure 5. (a) Normalized damping rate versus q_{95} for data with $|n| \leq 4$ (dark, $N_{tot} = 3150$) and $|n| \geq 5$ (light, $N_{tot} = 692$) in X-point configuration. Uncertainties are shown as error bars, and data are restricted to $\Delta(\gamma/\omega_0) \leq 0.5\%$. A linear fit to *all* data is overlaid. (b) Probability density functions of the normalized damping rate during external heating from NBI only ($N_{tot} = 395$), RF only ($N_{tot} = 1025$), or neither ($N_{tot} = 3592$). Note the logarithmic horizontal and vertical axes.

antenna operation must be carefully optimized for success in the upcoming high-performance DT campaign. That said, the AE antenna should have a higher chance of success during the 'afterglow' phase of some DT pulses, during which NBI and RF will purposefully be zeroed in order to isolate the effect of alpha drive.

Normalized damping rate measurements are shown as a function of the edge safety factor q_{95}, as determined by EFIT, in the scatter plot of figure 5(a). These data come only from resonances measured during X-point, or diverted, configuration of the magnetic geometry. Each data point is partially transparent, so that high density regions of parameter space are darker, e.g. $q_{95} \in [3, 6]$. Data are also distinguished by their estimated toroidal mode number: 'low' $|n| \leq 4$ (light in color) versus 'high' $|n| \geq 5$ (dark). Note that damping

rates for data with $|n| \leq 4$ tend to be greater than those with $|n| \geq 5$.

While there is significant spread in the data, we observe a general trend of increasing $|\gamma/\omega_0|$ as q_{95} increases. This is confirmed by a simple linear fit of *all* data, although the slope appears to be greater for data with $|n| \leq 4$ compared to $|n| \geq 5$. Increasing q_{95} - and thus changing the q-profile - can increase shear and continuum damping, leading to this trend. In previous studies of AE antenna data, the damping rate was found to increase with increasing q_{95}/q_0 and $q_{95} - q_0$ for $|n| = 3$ TAEs [30], but *decrease* with increasing q_{95} for $|n| = 7$ modes [29]. The latter result is not observed in this work, but may be due to poor statistics.

Because the uncertainty in the damping rate can be of the same order as the damping rate itself, i.e. $\Delta(\gamma/\omega_0) \sim |\gamma/\omega_0|$,

it is ill-advised to visualize these data in histograms. Instead, we can construct a smooth probability density function (pdf) in the following way: For a given data set, each measurement (data point) is assumed to be a Gaussian pdf $g(\mu_i, \sigma_i)$ with mean $\mu_i = \gamma/\omega_0$ and standard deviation $\sigma_i = \Delta(\gamma/\omega_0)$. Then, all individual pdfs from the data set are summed together, i.e. $G(\gamma/\omega_0) = \sum_i g(\mu_i, \sigma_i)$, and the total pdf is normalized so that the integral is 1. The probability of a measurement within a given range is therefore just the integral of the pdf over that range.

Three pdfs of the damping rate are shown in figure 5(b) for resonances detected during no external heating, only NBI, and only RF. With no heating, the pdf is peaked around $|\gamma/\omega_0| \approx 0.2\%$ and decreases exponentially as the damping rate increases. With only NBI heating, there is an increased probability of damping rate measurements near $|\gamma/\omega_0| \approx 0.3\% - 0.4\%$, which could be due to NBI ion Landau damping; damping rates above $|\gamma/\omega_0| > 0.5\%$ are less likely, however. A similar trend is seen for RF heating only: an increase in probability around $|\gamma/\omega_0| \approx 0.3\% - 0.7\%$, but a decrease beyond $|\gamma/\omega_0| > 0.7\%$. As mentioned previously, this decrease in high damping rate measurements could be due to AE drive from RF-heated fast ions.

5. Summary

In this paper, we summarized the operation of the Alfvén Eigenmode Active Diagnostic, or AE antenna, during the 2019-2020 JET deuterium campaign. Since its recent upgrade, six of the eight toroidally spaced antennas were independently powered and phased to excite stable MHD modes with frequencies spanning $f = 25$–250 kHz (see figure 1(a)) and toroidal mode numbers $|n| \leq 30$ (see figure 2(a)). Synchronously detected signals from fourteen fast magnetic probes (see table 1) were used to calculate mode parameters in a robust way: Resonant frequencies f_0 and damping rates γ were calculated as weighted means of all (at least three) probes' individual transfer function fits (see equation (1) and figure 3(b)). In general, resonant frequencies agree well with both estimated TAE frequencies and those calculated with MISHKA, although the match is better with the latter (see figure 1(b)). The damping rate was also corrected for time-varying AE antenna and resonant frequencies (see figure 3(a)).

For each resonance, the toroidal mode number was estimated in two ways, via (i) minimization of a weighted, reduced chi-square spectrum (see equation (2)) and (ii) maximization of the mode amplitude from sparse spectral decomposition (SparSpec, see equation (4)). Both methods were evaluated over the range of resolvable *n*, which depends on the positions of (at least three) probes with sufficiently good measurements of that resonance. While the discrete AE antenna system injects power into its own *n*-spectrum, a comparison of the dominant antenna-applied mode number and that estimated of the resonance showed good agreement (see figure 2(b)). In other words, the AE antenna successfully excited modes with similar mode number, or at least typically preserving parity. Most common were measurements of $n = 0$, which could be

true GAEs or caused by a superposition of modes. Observations of TAEs generally decreased with increasing *n* in $|n| \leq 10$ (see figure 2(a)). However, some modes with $10 < |n| \leq 30$ were measured with high confidence ($X > 3$ in equation (3) and $A > 3$ in equation (5)); these will be investigated in future work.

A database was constructed from resonances detected in 479 pulses spanning a wide range of plasma parameters (see table 3). Data were also filtered to reduce uncertainties and remove noise (see table 2). Several initial trends were observed: The probability of resonance detection decreases sharply for plasma currents $I_p > 2$ MA (see figure 4(a)); while this could simply be due to a decrease in the relative magnitude of the antenna's perturbation, there are also likely other conflating factors of high performance discharges. Furthermore, damping rates increase with the edge safety factor (see figure 5(a)), likely due to increased continuum damping. Finally, a competition between ion Landau damping and fast ion drive may be seen in two ways: First, the probability of resonance detection decreases as external heating power increases (see figure 4(b)), and damping rates $-\gamma/\omega_0 > 1\%$ are less likely when external heating is applied (see figure 5(b)).

This paper has laid the groundwork for many future studies utilizing this database, including statistical analyses of the bulk data as well as pulse identification for detailed analysis and comparison with modeling. Of particular interest will be the investigations high-*n* ($|n| \geq 7$) modes and their stability. In addition, isotope effects and, importantly, alpha drive will be explored as data is collected in the upcoming JET hydrogen, tritium, and DT campaigns. These data will be used to validate and improve the predictive capabilities of various MHD, kinetic, and gyrokinetic models. This is an important step in the assessment of energetic-particle-driven AEs and resulting AE-enhanced transport of energetic particles in future fusion devices.

Appendix A. Calculation of the maximum resolvable toroidal mode number

In this section, we will determine the range of distinguishable, or resolvable, toroidal mode numbers *n* for a given set of probe toroidal locations ϕ_k. This is related to non-uniform/aperiodic sampling of the discrete Fourier transform.

Consider a toroidal array of N fast magnetic probes located at different toroidal angles $\phi_k \in [0, 2\pi)$ for $k \in [1, N]$. For simplicity, let all probes have the same radial and poloidal position, and let $\phi_1 = 0$. For a magnetic perturbation with toroidal mode number n, the phase of the (appropriately-filtered) signal of probe k is $\theta_k = n\phi_k \in [0, 2\pi)$.

Consider two toroidal mode numbers n_i and n_j, with $n_i > n_j$. The signals produced by these two modes will be *indistinguishable* if,

$$\mathrm{mod}\,(n_i\phi_k, 2\pi) - \mathrm{mod}\,(n_j\phi_k, 2\pi) = 0, \quad \forall \phi_k. \tag{A1}$$

Here $\mathrm{mod}\,(\cdot, 2\pi)$ is the modulo operator on 2π. Another way to write this operator is

$$\mathrm{mod}\,(\theta_k, 2\pi) = \mathrm{atan2}\left(\frac{\sin\theta_k}{\cos\theta_k}\right) \tag{A2}$$

where $\mathrm{atan2}\,(\cdot) \in [0, 2\pi)$ is the arctangent function in four quadrants. One property of this function is

$$\mathrm{atan2}\left(\frac{y_i}{x_i}\right) \pm \mathrm{atan2}\left(\frac{y_j}{x_j}\right) = \mathrm{atan2}\left(\frac{y_i x_j \pm y_j x_i}{x_i x_j \mp y_i y_j}\right). \tag{A3}$$

Let $\theta_i = n_i\phi_k$, $x_i = \cos\theta_i$, $y_i = \sin\theta_i$, and the same for θ_j, x_j, and y_j (where we have dropped the subscript k). Combining equations (A1), (A2), and using the angle summation trigonometric identities, our indistinguishability condition becomes

$$\mathrm{atan2}\left(\frac{\sin(\theta_i - \theta_j)}{\cos(\theta_i - \theta_j)}\right) = \mathrm{mod}\,((n_i - n_j)\phi_k, 2\pi) = 0, \quad \forall \phi_k. \tag{A4}$$

We only need one probe location which does not satisfy equation (A4) for toroidal mode numbers n_i and n_j to be distinguishable.

Presume that all ϕ_k are some rational fraction of 2π.[10] Then there exists $n^* = n_i - n_j$ (along with its integer multiples) which satisfies equation (A4) for all ϕ_k. For a given n^*, we want to *minimize* both $|n_i|$ and $|n_j|$; these are then the *smallest* mode numbers which are indistinguishable. Pairs including higher values can also be indistinguishable, but are the result of aliasing. By inspection, we can minimize both $|n_i|$ and $|n_j|$ by setting $n_j = -n_i$. Thus, we conclude that the *maximum resolvable toroidal mode number* is $n_{max} = \lfloor n^*/2 \rfloor$, with $\lfloor \cdot \rfloor$ the floor operator. Note that this satisfies the Nyquist theorem for probes with uniform separation $\Delta\phi = 2\pi/n^*$.

It is *not* always the case that both $\pm n_{max}$ can be distinguished. This must be checked separately. Hence, the range of resolvable toroidal mode number is either $n \in [-n_{max}, \ldots, n_{max}]$ or $[-n_{max} + 1, \ldots, \pm n_{max}]$, where $\pm n_{max}$ is treated as 'one' toroidal mode number.

To determine n_{max} from ϕ_k, we use the above reasoning to require that each $\phi_k/2\pi = m_k/2n_{max}$ is a rational number, with m_k non-negative integers. (Recall that we set $\phi_1 = 0$ so that

$m_1 = 0$.) Then, n_{max} can be determined by finding the lowest common denominator of all ϕ_k/π, which can be computed by various algorithms.

ORCID iDs

R A Tinguely ● https://orcid.org/0000-0002-3711-1834
A Fasoli ● https://orcid.org/0000-0003-4319-5736

References

[1] Fasoli A *et al* 2007 Chapter 5: Physics of energetic ions *Nucl. Fusion* **47** S264–S284
[2] Greenwald M *et al* 2018 The high-field path to practical fusion energy (https://doi.org/10.7910/DVN/OYYBNU)
[3] Fasoli A *et al* 1995 Direct measurement of the damping of toroidicity-induced Alfvén eigenmodes *Phys. Rev. Lett.* **75** 645–8
[4] Puglia P *et al* 2016 The upgraded JET toroidal Alfvén eigenmode diagnostic system *Nucl. Fusion* **56** 112020
[5] Fasoli A *et al* 1995 Overview of Alfven eigenmode experiments in JET *Nucl. Fusion* **35** 1485
[6] Fasoli A *et al* 1996 Observation of Multiple Kinetic Alfvén Eigenmodes *Phys. Rev. Lett.* **76** 1067
[7] Fasoli A *et al* 1997 Alfven eigenmode experiments in tokamaks and stellarators *Plasma Phys. Control. Fusion* **39** 287–301
[8] Heidbrink W W, Fasoli A, Borba D and Jaun A 1997 Stable ellipticity-induced Alfvén eigenmodes in the Joint European Torus *Phys. Plasmas* **4** 3663
[9] Jaun A, Fasoli A and Heidbrink W W 1998 Prediction of Alfvén eigenmode dampings in the Joint European Torus *Phys. Plasmas* **5** 2952–5
[10] Wong K L 1999 A review of Alfvén eigenmode observations in toroidal plasmas *Plasma Phys. Control. Fusion* **41** R1–R56
[11] Fasoli A, Borba D, Breizman B, Gormezano C, Heeter R F, Juan A, Mantsinen M, Sharapov S and Testa D 2000 Fast particles-wave interaction in the Alfvén frequency range on the Joint European Torus tokamak *Phys. Plasmas* **7** 1816–24
[12] Fasoli A, Jaun A and Testa D 2000 Isotope mass scaling of AE damping rates in the JET tokamak plasmas *Phys. Lett.* A **265** 288–93
[13] Jaun A, Fasoli A and Vaclavik J 2001 Gyrokinetic modelling of macro-instabilities in high performance tokamak plasmas *Plasma Phys. Control. Fusion* **43** 207
[14] Testa D and Fasoli A 2001 The effect of plasma shaping on the damping of low n Alfvén eigenmodes in JET tokamak plasmas *Nucl. Fusion* **41** 809–12
[15] Fasoli A, Testa D, Sharapov S, Berk H L, Breizman B, Gondhalekar A, Heeter R F, Mantsinen M and contributors to the EFDA-JET Workprogramme 2002 MHD spectroscopy *Plasma Phys. Control. Fusion* **44** B159–B172
[16] Testa D, Fasoli A, Jaun A, Gorelenkov N N, Berk H L, Budny R, Boswell C and Albarracin M A 2003 Experimental test of damping models for n=1 toroidal Alfvén eigenmodes in JET *Nucl. Fusion* **43** 479–82
[17] Testa D, Fasoli A and Jaun A 2003 Measurement of the damping rate of toroidal Alfvén eigenmodes as a function of the neutral beam heating power and plasma β on JET *Nucl. Fusion* **43** 724–8
[18] Testa D, Fasoli A and Solano E 2003 Diagnosis and study of Alfvén eigenmodes stability in JET (invited) *Rev. Sci. Instrum.* **74** 1694–700 American Institute of Physics

---

[10] This is not a bad assumption since there will always be some error in our measurement. Thus, we actually require that equation (A4) be less than some uncertainty in the phase, instead of exactly zero.

[19] Testa D, Boswell C, Fasoli A, Borba D, de Baar M, Bigi M, Brzozowski J, de Vries P and Contributors JET-EFDA 2004 Alfvén mode stability and wave-particle interaction in the JET tokamak: prospects for scenario development and control schemes in burning plasma experiments *Plasma Phys. Control. Fusion* **46** 59–79

[20] Testa D, Boswell C and Fasoli A 2005 Experimental study of the dependence of the damping rate of n < 1 TAEs on the on-axis safety factor and toroidal rotation shear *Nucl. Fusion* **45** 907–17

[21] Testa D, Boswell C, Fasoli A and Contributors JET-EFDA 2006 Measurement of the instability threshold for toroidal Alfvén eigenmodes in JET plasmas with forward and reversed magnetic field *Nucl. Fusion* **46** 829–36

[22] Klein A, Carfantan H, Testa D, Fasoli A and Snipes J 2008 A sparsity-based method for the analysis of magnetic fluctuations in unevenly-spaced Mirnov coils *Plasma Phys. Control. Fusion* **50** 125005

[23] Fasoli A, Testa D, Panis T, Klein A, Snipes J A, Sears J, Gryaznevich M, Martin R and Pinches S D 2010 Active excitation and damping rate measurement of intermediate-n toroidal Alfvén eigenmodes in JET, C-Mod and MAST plasmas *Plasma Phys. Control. Fusion* **52** 075015

[24] Panis T, Testa D, Fasoli A, Klein A, Carfantan H, Blanchard P and Contributors JET-EFDA 2010 Optimization of the active MHD spectroscopy system on JET for the excitation of individual intermediate and high-n Alfvén eigenmodes *Nucl. Fusion* **50** 084019

[25] Testa D, Mellet N, Panis T, Blanchard P, Carfantan H, Fasoli A and Contributors J-EFDA 2010 The dependence of the damping rate of medium-n toroidal Alfven eigenmodes on the edge plasma elongation in JET *Nucl. Fusion* **50** 084010

[26] Testa D, Carfantan H, Goodyear A, Blanchard P, Klein A, Panis T and contributors JET-EFDA 2010 The JET Alfvén Eigenmode Local Manager for the real-time detection and tracking of MHD instabilities *Lett. Journal Exploring Front. Phys.* **92** 50001

[27] Testa D, Spong D, Panis T, Blanchard P, Fasoli A and JET-EFDA Contributors 2011 Recent JET experiments on Alfvén eigenmodes with intermediate toroidal mode numbers: measurements and modelling of n = 3 toroidal Alfvén eigenmodes with the TAEFL code *Nucl. Fusion* **51** 43009–20 JET-EFDA Contributors

[28] Testa D, Carfantan H, Fasoli A, Goodyear A, King Q, Blanchard P, Klein A, Lavanchy P and Panis T 2011 The JET Alfvén Eigenmode Local Manager for the real-time detection and tracking of a frequency-degenerate spectrum of MHD instabilities *Fusion Eng. Des.* **86** 381–92

[29] Panis T, Fasoli A and Testa D and JET-EFDA Contributors 2012 Analysis of damping rate measurements of toroidal Alfven eigenmodes on JET as a function of n: part I *Nucl. Fusion* **52** 23013–27

[30] Panis T, Fasoli A and Testa D 2012 Analysis of damping rate measurements of toroidal Alfvén eigenmodes as a function of n: Part II *Nucl. Fusion* **52** 023014

[31] Testa D, Panis T, Blanchard P, Fasoli A and JET-EFDA Contributors 2012 Plasma isotopic effect on the damping rate of toroidal Alfvén eigenmodes with intermediate toroidal mode numbers *Nucl. Fusion* **52** 094006

[32] Testa D, Carfantan H and Goodyear A 2014 Implementation of a novel real-time controller for the detection and tracking of magneto-hydrodynamic instabilities on the JET tokamak *Plasma Fusion Res.* **9** 1–46

[33] Nabais F *et al* 2018 TAE stability calculations compared to TAE antenna results in JET *Nucl. Fusion* **58** 082007

[34] Aslanyan V *et al* 2019 Gyrokinetic simulations of toroidal Alfvén eigenmodes energetic ions and external antennas on the Joint European Torus *Nucl. Fusion* **59**

[35] Fasoli A, Testa D, Way M, Walton R, Sanders S and Riccardo V *et al* 2003 The new alfvén wave excitation system at jet *8th IAEA Technical Committee Meeting on Energetic Particles in Magnetic Confinement Systems*, San Diego, USA 026008

[36] Testa D *et al* 2004 The new TAE-Alfvén wave active excitation system at JET *Proc. 23rd Symp. on Fusion Technology (SOFT)*, Venice (Italy) 20–4

[37] Mikhailovskii A B, Huysmans G T A, Kerner W O K and Sharapov S E 1997 Optimization of computational MHD normal-mode analysis for tokamaks *Plasma Phys. Rep.* **23** 844–57

[38] Moret J-M 1994 Fitting of transfer functions to frequency response measurements *Technical report* Centre de Recherches en Physique des Plasmas

[39] Gatz D F and Smith L 1995 The standard error of a weighted mean concentration—I. Bootstrapping vs other methods *Atmos. Environ.* **29** 1185–93

[40] Huysmans G T A, Goedbloed J P and Kerner W 1991 Isoparametric Bicubic Hermite Elements for Solution of the Grad-Shafranov Equation *Int. J. Mod. Phys.* **02** 371–6

[41] Lao L L, St John H, Stambaugh R D, Kellman A G and Pfeiffer W 1985 Reconstruction of current profile parameters and plasma shapes in tokamaks *Nucl. Fusion* **25** 1611–22

[42] Huysmans G T A, Sharapov S E, Mikhailovskii A B and Kerner W 2001 Modeling of diamagnetic stabilization of ideal magnetohydrodynamic instabilities associated with the transport barrier *Phys. Plasmas* **8** 4292–305

[43] Todo Y 2019 Introduction to the interaction between energetic particles and Alfven eigenmodes in toroidal plasmas *Rev. Modern Plasma Phys.* **3** 1

[44] Dumont R J *et al* 2018 Scenario development for the observation of alpha-driven instabilities in JET DT plasmas *Nucl. Fusion* **58** 082005

[45] Bourguignon S, Carfantan H and Böhm T 2007 SparSpec: A new method for fitting multiple sinusoids with irregularly sampled data *Astron. Astrophys.* **462** 379–87

[46] Ross D W, Chen G L and Mahajan S M 1982 Kinetic description of Alfvén wave heating *Phys. Fluids* **25** 652–67

[47] Appert K, Gruber R, Troyuon F and Vaclavik J 1982 Excitation of global eigenmodes of the Alfven wave in Tokamaks *Plasma Phys.* **24** 1147–59

[48] Oliver H J C, Sharapov S E, Breizman B N, Zheng L-J and Contributors J 2017 Axisymmetric global Alfvén eigenmodes within the ellipticity-induced frequency gap in the Joint European Torus *Phys. Plasmas* **24** 122505

[49] Tinguely R A *et al* 2020 Experimental studies of plasma-antenna coupling with the JET Alfvén Eigenmode Active Diagnostic In progress